JACS
JOURNAL OF THE AMERICAN CHEMICAL SOCIETY
Article
pubs.acs.org/JACS

Solvothermal Synthesis of Platinum Alloy Nanoparticles for Oxygen Reduction Electrocatalysis

Michael K. Carpenter,*[,†] Thomas E. Moylan,[†] Ratandeep Singh Kukreja,[‡] Mohammed H. Atwan,[‡] and Misle M. Tessema[§]

[†]Electrochemical Energy Research Lab, General Motors R&D Center, Warren, Michigan 48090, United States
[‡]Trison Business Solutions, Inc., 17 Bank Street, LeRoy, New York 14482, United States
[§]Optimal Computer Aided Engineering, Inc., 14492 North Sheldon Road, Suite 300, Plymouth, Michigan 48170, United States

Supporting Information

ABSTRACT: Platinum alloy nanoparticles show great promise as electrocatalysts for the oxygen reduction reaction (ORR) in fuel cell cathodes. We report here on the use of *N*,*N*-dimethylformamide (DMF) as both solvent and reductant in the solvothermal synthesis of Pt alloy nanoparticles (NPs), with a particular focus on Pt−Ni alloys. Well-faceted alloy nanocrystals were generated with this method, including predominantly cubic and cuboctahedral nanocrystals of Pt_3Ni, and octahedral and truncated octahedral nanocrystals of PtNi. X-ray diffraction (XRD) and high angle annular dark field scanning transmission electron microscopy (HAADF-STEM), coupled with energy dispersive spectroscopy (EDS), were used to characterize crystallite morphology and composition. ORR activities of the alloy nanoparticles were measured with a rotating disk electrode (RDE) technique. While some Pt_3Ni alloy nanoparticle catalysts showed specific activities greater than 1000 $\mu A/cm^2_{Pt}$, alloy catalysts prepared with a nominal composition of PtNi displayed activities close to 3000 $\mu A/cm^2_{Pt}$, or almost 15 times that of a state-of-the-art Pt/carbon catalyst. XRD and EDS confirmed the presence of two NP compositions in this catalyst. HAADF-STEM examination of the PtNi nanoparticle catalyst after RDE testing revealed the development of hollows in a number of the nanoparticles due to nickel dissolution. Continued voltage cycling caused further nickel dissolution and void formation, but significant activity remained even after 20 000 cycles.

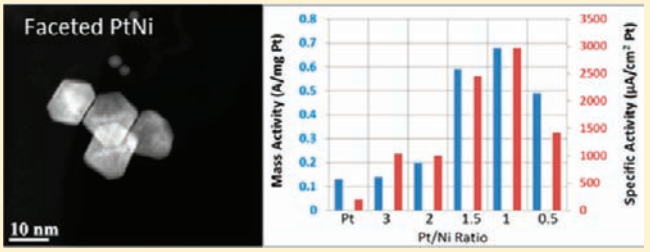

INTRODUCTION

The platinum content of automotive fuel cells must be reduced if this technology is to become economically viable. Because most of the platinum is used in the cathode as an electrocatalyst for the oxygen reduction reaction (ORR), decreasing the amount of platinum in this electrode is of primary importance in any platinum reduction strategy. Unfortunately, the demands of the complex 4-electron ORR and the acidic environment of the fuel cell electrode pose major barriers to the outright replacement of platinum by a less-expensive metal. Therefore, the current reduction strategy is to improve the average catalytic activity of the platinum atoms contained within a catalyst. Specifically, platinum mass activity must be increased by at least a factor of 4 if suggested automotive cost targets[1] are to be met.

One of the most-studied approaches to improved catalyst activity is the use of Pt alloy nanoparticles (NPs) in place of pure Pt NPs. While many alloy NP catalysts have shown improved activities, the amount of improvement has typically been only a factor of 2−3.[2−4] More encouraging results have been obtained recently from systems with controlled compositional structures and/or particle morphologies. Core−shell structured materials of various types have shown much promise in this regard, including Pt and Pt alloy monolayer or multilayer nanoparticle catalysts[5−7] and the nanostructured thin film (NSTF) system described by Debe and co-workers.[8,9] One interesting lead in the development of active cathode catalysts was recently reported by Stamenkovic and co-workers,[10] who found that the (111) surface of Pt_3Ni (bulk single crystal) exhibits an extremely high specific activity for ORR, about 90 times greater than the Pt nanoparticles used in conventional catalysts. While large single crystals do not have sufficient surface area to be viable fuel cell catalysts, Pt_3Ni nanocrystals with exposed (111) faces might prove to be excellent ORR catalysts for fuel cells; therefore, the synthesis of Pt_3Ni nanoparticles with controlled morphologies is a topic of great interest. In particular, for this face-centered cubic (fcc) alloy system, octahedral or tetrahedral nanocrystals are desirable because all of their facets are (111) surfaces. Recently, two groups have reported promising syntheses of Pt_3Ni nanocrystals with preferential faceting. Yang and co-workers reported the synthesis of truncated octahedral Pt_3Ni nanocrystals,[11] while Fang and co-workers[12] developed a synthesis and separation

Received: January 23, 2012
Published: April 23, 2012

   dx.doi.org/10.1021/ja300756y | *J. Am. Chem. Soc.* 2012, 134, 8535−8542

procedure to obtain a product of predominantly Pt_3Ni nanooctahedra. While the ORR activities of both materials are promising, comparison with the reported activity of the extended Pt_3Ni surface suggests that still greater improvements can be achieved.

Most synthetic methods used to make well-faceted nanocrystals use strongly adsorbing molecules as so-called capping agents to direct the reaction and crystal growth pathway(s) to yield particles with the desired geometry. Unfortunately, these capping agents remain strongly adsorbed on the particle surfaces even after the synthesis is complete and must be removed if the NPs are to be usable as catalysts. Indeed, full removal of the capping agent(s) without altering the NP structure can be a challenging problem in itself. We report here on a novel, simple method of synthesizing well-faceted Pt alloy nanoparticles without the use of capping agents. Specifically, we report a solvothermal method in which DMF functions as both solvent and reductant. While aqueous DMF solutions have previously been used to generate gold and silver nanoparticles,[13,14] we believe this is the first report of the use of neat DMF as a reductant to produce Pt and Pt alloy nanoparticles. With this method, we have generated NPs with a range of Pt alloy compositions and geometries, some of which show very promising ORR catalytic activity.

EXPERIMENTAL SECTION

Synthesis. Platinum alloy nanocrystals were generated by solvothermal reactions using DMF (99.8+%, Alfa Aesar) in a sealed, PTFE-lined vessel (Parr Instrument Co., acid digestion vessel 4749). The metal precursors were acetylacetonate compounds, specifically, platinum(II) 2,4-pentanedionate (Gelest), nickel(II) 2,4-pentanedionate (Alfa Aesar), cobalt(II) acetylacetonate hydrate (Strem Chemicals), cobalt(III) acetylacetonate (Strem), chromium(III) acetylacetonate (Strem), and iron(III) acetylacetonate (Acros Organics). Initial reactions to determine reduction temperatures were carried out in 10 mL glass vials with PTFE-lined screw caps. In a typical synthesis, Pt and Ni acetylacetonates were dissolved in 12 mL of DMF to yield concentrations of 30 mM $Pt(acac)_2$ and 10 mM $Ni(acac)_2$. The reaction mixture was sealed in the PTFE-lined vessel and heated in a furnace to 200 °C for 24 h. The vessel was then removed from the furnace and allowed to cool to ambient temperature before opening. To minimize nanoparticle aggregation, the alloy nanoparticles were supported on carbon (Ketjenblack, EC-300J). The product mixture was sonicated in an ultrasonic cleaner for 30 min and was then added to 25 mL of ethanol in which 0.15 g of carbon had been dispersed by 30 min of sonication. The combined mixture was sonicated for another 30 min and then stirred for several hours. The solids were separated from the mixture by centrifugation, and the clear yellow supernatant liquid was removed. The remaining traces of DMF and unwanted reaction products were removed from the solids with three "wash cycles": two with ethanol (Aldrich, denatured with isopropanol) and the last with acetone (99.0%, EM Science). Each cycle consisted of dispersing the solids in ~25 mL of solvent by sonication and/or stirring, followed by centrifugation and removal of the supernatant. The solids were removed from the final wash by filtration rather than centrifugation and were rinsed briefly with acetone and rinsed several times with water. The catalyst was vacuum-dried overnight, collected, and weighed.

Chemical and XRD Characterization. Dried catalyst powders were wet-ashed utilizing perchloric acid ($HClO_4$ BDH Aristar Trace Metal grade), and analyzed by a Varian 725-ES inductively coupled plasma optical emission spectrometer (ICP-OES) calibrated with an in-house prepared platinum standard with a concentration of approximately 3 mg/mL. The accuracy and precision of this analysis is within 1−3% of the reported value on a relative basis.

X-ray diffraction (XRD) data were collected on a D8-Advance Davinci diffractometer in a parallel-beam configuration using copper K_α radiation. Data were collected from 30° to 90° 2θ at a fixed incidence angle of 4° using a 0.04° step size and an integration time of 2 s/step. Phases were identified by comparing the observed data to reference data from the International Centre for Diffraction Data (ICDD). Lattice parameters were calculated from the diffraction peak angle using Bragg's Law. Alloy compositions were calculated from the lattice parameter using Vegard's law.[15] Crystallite size was estimated according to Scherrer's equation.

HAADF-STEM and STEM-EDS Characterization. High angle annular dark field scanning transmission electron microscopy (HAADF-STEM) images were taken of samples supported on lacey carbon grids in a C_s-corrected JEOL 2100F TEM/STEM operated at 200 keV. Catalyst films were removed from RDEs for TEM by briefly sonicating them in about 5 mL of methanol. The catalyst particles thus removed were diluted further in methanol and sonicated for TEM sample preparation.

Energy dispersive spectroscopy (EDS) in the STEM mode was employed for elemental composition and distribution of the catalyst particles. The overall composition of individual/aggregated particles was measured using either a point or an area scan. The distribution (nonquantitative) of the elements within a single particle was determined by identification of the elemental peaks observed in the EDS spectrum at each pixel during mapping.

Electrochemical Measurements. Electrochemical measurements were made at room temperature with a thin film rotating disk electrode (TF-RDE) technique similar to that reported by Schmidt et al.[16] Thin films were prepared on 5 mm glassy carbon disks by applying a measured amount (between 10 and 20 μL) of an aqueous catalyst ink comprising 0.5−1.0 mg catalyst mL^{-1} with 1−5 $\mu L/mg_{catalyst}$ of 11 wt % Nafion solution (DuPont) and allowing them to air-dry. Platinum loadings were in the range of 15−20 $\mu g/cm^2$. A Pyrex electrochemical cell was filled with about 0.1 L of 0.1 M $HClO_4$ (GFS Chemicals) and covered with a Teflon cap. A reversible hydrogen electrode (RHE) reference was placed in a separate beaker and connected to the cell by a bridge tube, and the beaker, bridge, and RHE were all filled with the same electrolyte. A Luggin capillary effectively placed the reference about 1 cm from the thin-film working electrode. The counter electrode was a platinum mesh connected to the cell through a coarse glass frit. All potentials were referenced to the RHE, a trapped hydrogen bubble electrode, which was periodically calibrated by saturating the cell with 1 atm $H_2(g)$ and measuring the open-circuit potential of the working electrode directly. This procedure has been shown to give equivalent results to measuring the zero-current crossing point of the hydrogen evolution/oxidation reaction on the working electrode.

The electrode film was immersed in the Pt double-layer region (+500 mV) after the electrolyte was saturated with argon and was cycled 400 times between 50 and 950 mV at 1 V/s to yield a stable current−voltage curve. Three additional voltage cycles were then run at 20 mV/s, and the Pt electrochemical surface area (ECSA) was estimated from the charge of the underpotentially deposited (UPD) hydrogen, assuming 210 $\mu C/cm^2_{Pt}$.

With the film poised in the double-layer region, oxygen was sparged for a minimum of 30 min to initially saturate the electrolyte and then continuously throughout the ORR measurement. At successive rotation speeds of 100, 400, 900, and 1600 rpm, the film was initially held at +150 mV for 60 s and then swept anodically to +950 mV at 5 mV/s. The geometric current measured at 900 mV was corrected using the diffusion current through the hydrodynamic boundary layer to estimate the kinetic current, $1/i_K = 1/i_{geo} - 1/i_{lim}$, and the catalyst activity was calculated from this kinetic current. We report i_K at 1600 rpm because the films are sufficiently thin that the effects of diffusion through the film can be ignored. Reported activities are average values obtained from measurements on three separate films.

RESULTS AND DISCUSSION

Solvothermal Synthesis. While DMF is known to be a versatile solvent, its role as a mild reducing agent has been much less studied. Recent reports of the generation of silver

and gold nanocrystals, from the reduction of appropriate metal precursors by DMF,[13,14,17,18] revealed its reducing capability in aqueous solutions at elevated temperatures. Here, we use neat DMF in a solvothermal method to generate platinum alloy nanocrystals.

Preliminary experiments to determine the approximate minimum reaction temperatures required for the reduction of the platinum and nickel metal precursors were performed with sealed glass vials of DMF solutions containing known amounts of only $Pt(acac)_2$, only $Ni(acac)_2$, or a mixture of the precursors in a 3/1 Pt/Ni molar ratio. Typically 6 mL of the desired solution was measured into each vial. The vials were heated in an oil bath, and the temperature was slowly increased. The approximate reaction onset temperature within a vial was noted visually by a darkening of the reaction mixture due to the generation of metal NPs from the reduction of the metal precursor(s). Once a reaction was seen to begin, the temperature was stabilized, and the vial was allowed to react for 24 h at that temperature. Reactions were also conducted with the various precursor solutions held at 200 °C in a PTFE-lined stainless steel cell for 24 h. The reaction products were washed with ethanol and supported on a measured amount of carbon. The metal contents of these carbon-supported products were determined by ICP-OES, and the metal reduction efficiencies (RE) for the corresponding reaction conditions were calculated on the basis of analyzed metal content versus the expected metal content for a complete reduction. These reduction efficiencies are listed in Table 1.

Table 1. DMF Reduction Efficiencies of $Pt(acac)_2$ and $Ni(acac)_2$ after 24 h at Selected Temperatures

reactant concn (mM)	reaction temp (°C)	Pt RE (%)	Ni RE (%)
Ni(30)	200		31
Ni(10)	200		42
Pt(30)	200	91	
Pt(30)	137	11	
Pt(30), Ni(10)	115	83	48
Pt(30), Ni(10)	200	97	90

As expected, $Ni(acac)_2$ was more difficult to reduce than $Pt(acac)_2$ and did not react up to the maximum temperature used with the vials (150 °C). To safely access higher temperatures, the $Ni(acac)_2$-only solution was sealed in a PTFE-lined cell and heated to 200 °C for 24 h. A comparison of the product compositions from the two reactions containing 10 mM $Ni(acac)_2$ and reacted at 200 °C shows that only 42% of the Ni precursor in the Ni-only reaction was reduced, while 90% was reduced when $Pt(acac)_2$ was included in the mixture. This suggests that the presence of Pt and/or $Pt(acac)_2$ enhances the deposition of Ni. Interestingly, the converse also appears to hold because the apparent reaction onset temperature of the mixed precursor solution (115 °C) was lower than that of the $Pt(acac)_2$-only solution (137 °C). Further, a much larger proportion of Pt was deposited from the mixed solution heated at the lower temperature than was deposited from the Pt-only solution reacted at 137 °C. These observations suggest that the free energy of formation of the platinum–nickel alloy NPs from the reaction mixture is more negative than the free energy of formation of platinum NPs from the same solution. Alternatively, it may be that under these reaction conditions Pt proto-particles of only a few atoms are formed initially and act as seed crystals for subsequent Ni and Pt_3Ni deposition. This latter hypothesis is in accord with the finding by Deivaraj et al. that the reduction of nickel ions by hydrazine at room temperature requires the presence of platinum nuclei.[19] Similarly, Moffat and co-workers[20] attributed the electro-codeposition of Pt and Ni at potentials positive of the reduction potential of Ni to the underpotential deposition of Ni on Pt nanoparticle surfaces.

Figure 1 shows the XRD spectra of products obtained from a series of solvothermal reactions with a platinum-to-nickel precursor ratio of 3 and heated at 200 °C for lengths of time varying from 1 to 24 h. The relative peak heights suggest that the reaction is essentially complete within 4–6 h. Subsequent analyses of the products indicate that about 25–30% of the metal precursors were reduced within the first hour, with 80–85% reduced by the end of the second hour. XRD shows the products to be well-alloyed Pt alloy NPs comprising a single fcc phase. A comparison of the analyzed Pt/Ni ratios of the products with the ratios estimated from the XRD data using Vegard's Law reveals that these XRD-derived ratios are typically somewhat greater than the analyzed ratios (see the Supporting Information). This discrepancy may be due to the presence of a small amount of amorphous nickel or oxidized nickel phases in the product mixtures.

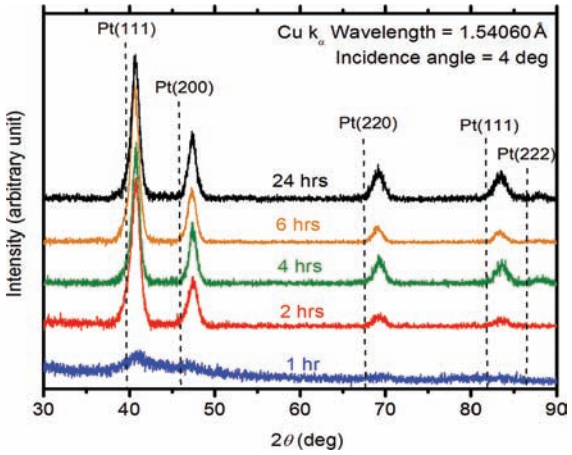

Figure 1. XRD spectra of C-supported Pt_3Ni products from DMF reactions conducted at 200 °C for 1, 2, 4, 6, and 24 h.

Morphology of Pt_3Ni Nanoparticles. TEM pictures of the Pt_3Ni products show most of the NPs to be well-faceted crystals with a predominance of cubes and cuboctahedra, as shown in Figure 2. This simple synthesis of such well-faceted nanocrystals is somewhat unusual, as most common synthetic methods yield spherical or irregularly shaped NPs. While some syntheses of well-faceted platinum and platinum alloy NPs of specific shapes have been reported, such reactions have typically utilized capping agents such as polyvinylpyrrolidone[21] or oleylamine[12] to control the course of particle development. The lower panel of Figure 2 shows an isolated, well-formed cubic nanocrystal, while the upper panel shows an agglomeration of nanocrystals made up of similar well-faceted nanocubes and cuboctahedral structures. Estimates of average NP particle size from TEM micrographs range from 11 to 13 nm, slightly more than double the average crystallite size estimates calculated for the same samples using XRD data and the Scherrer equation (Supporting Information). These differing estimates could be reconciled if the NPs were made up of two or more crystallites; however, this seems unlikely given the

dx.doi.org/10.1021/ja300756y | J. Am. Chem. Soc. 2012, 134, 8535–8542

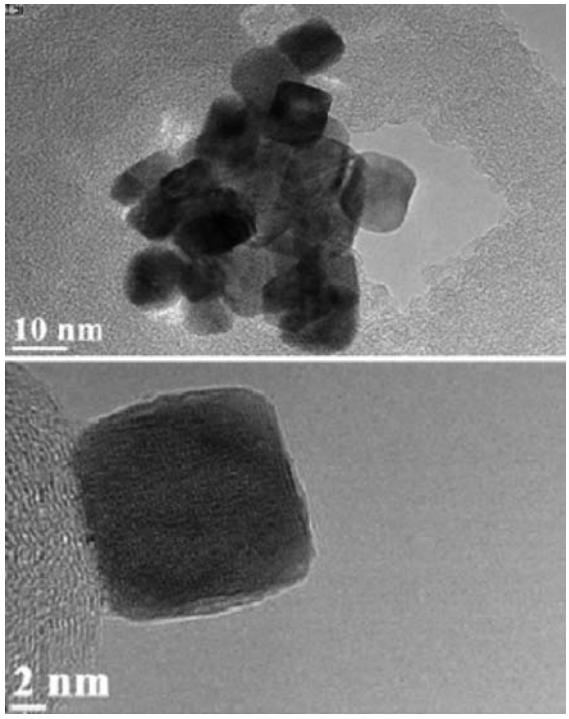

Figure 2. Bright-field TEMs of Pt_3Ni nanoparticles obtained from a 24 h solvothermal DMF reaction.

simple cubic and cuboctahedral particle shapes, which suggest single-crystalline particles. Alternatively, the agglomerates may harbor smaller crystallites in their interiors that contribute significantly to the XRD size estimates, although the relative lack of individual particles seen in this size range argues against this explanation as well. Finally, there is also the possibility that the XRD estimate is affected by the presence of a range of Pt–Ni particle compositions, which would serve to broaden the diffraction peaks and lead to a smaller crystallite size estimate from the Scherrer equation.

From Figure 2 and similar micrographs (not shown), it seems that the sizes of the alloy NPs do not vary widely, with most occurring in the range of 9–17 nm. This relatively narrow size distribution is probably a result of a particle formation process that begins with an initial homogeneous nucleation step followed by continued growth on the nuclei as the reduction of the metal precursors proceeds. As the reactant temperature is increased, homogeneous nucleation likely occurs simultaneously throughout the solution volume when the reducing power of the DMF reaches a critical level, as determined by the solution temperature. The resulting rapid decrease in precursor concentration coupled with the availability of the newly formed crystal seeds would then favor subsequent crystal growth over continued nucleation. The crystal seeds, formed at the same time throughout the solution volume, would then proceed to grow at the same rate for the length of the reaction to produce a uniform particle size.

Synthesis and Morphology of Pt_3M Nanoparticles (M ≠ Ni). Platinum alloys with first row transition metals other than nickel were also synthesized by the DMF solvothermal method. Reaction conditions analogous to those used to synthesize Pt_3Ni NPs were used to generate Pt–M alloy NPs where M is Co, Cu, or Fe. The appropriate DMF solutions of metal acetylacetonate precursors with a Pt/M mole ratio of 3 were heated in a sealed cell to 200 °C for 6 h, and the NPs were subsequently supported on carbon. For cobalt, both Co(II) and Co(III) acetylacetonates were used in separate alloy syntheses. Cr(III) acetylacetonate could not be reduced under these conditions.

Table 2 shows the metal contents of the C-supported products, as determined by ICP-OES. As with the Pt–Ni system, most of both metal precursors were reduced, with a somewhat larger fraction of the Pt ions reduced than the non-noble metal ions. This is seen in the product Pt/M ratios that are typically slightly greater than the precursor Pt/M ratio of 3, with the reaction involving Co(II) being the lone exception. XRD scans of the supported catalysts show all of the Pt_3M reaction products to have fcc structures. From the measured lattice parameters and using Vegard's Law, the mole fractions of the metals in the NPs can be estimated and are listed in Table 2. As with the Pt_3Ni NPs, the Pt/M ratios obtained from this calculation are greater than the analyzed Pt/M ratios. Again, this difference may be due to the presence of amorphous or oxidized metal phases. The extremely high Pt/Cu ratio found for the Pt–Cu NPs indicates that very little alloying occurred between the Cu and Pt in this synthesis. The absence of diffraction peaks from any crystalline phase associated with copper clearly indicates that this sample contains a significant amount of an amorphous Cu-containing phase, perhaps copper oxide.

From the HAADF-STEM images in Figure 3, it can be seen that all of the Pt–M syntheses generated well-faceted nanoparticles, except for Pt–Fe. Both Pt–Co syntheses gave predominantly cuboctahedral crystals with reasonably narrow particle size distributions, centered about 12 and 10 nm for the syntheses using the Co(II) and Co(III) precursors, respectively. The NPs obtained from the Pt–Cu reaction, largely Pt, are generally well-faceted, but show more diversity in particle shape and size than either the Pt_3Ni or the Pt_3Co products. Despite the similarity of reaction conditions, the Pt–Fe NPs obtained are not well-faceted, but instead display more curved surfaces. The reason(s) for this difference in behavior is unclear.

Morphological Effects of Varying Pt/Ni Ratio. A series of solvothermal reactions were carried out with Pt/Ni reactant ratios varying from 3 to 0.5. The analyzed Pt/Ni product ratios were generally slightly greater than the reactant ratios,

Table 2. Metal Contents and XRD Characterization of C-Supported Products from Pt/M = 3 Reactions

	ICP analyzed content			XRD-derived composition estimates			
M precursor	Pt (wt %)	M (wt %)	Pt/M atomic ratio	lattice parameter	Pt mole fraction	M mole fraction	Pt/M mole ratio
$Ni(acac)_2$	27	2.6	3.1	3.8435	0.80	0.20	4.0
$Co(acac)_2$	29	3.2	2.7	3.8464	0.80	0.20	4.0
$Co(acac)_3$	28	2.7	3.1	3.8337	0.76	0.24	3.2
$Cu(acac)_2$	27	2.7	3.3	3.9195	0.99	0.01	99.0
$Fe(acac)_3$	26	2.2	3.3	3.8696	0.85	0.15	5.6

dx.doi.org/10.1021/ja300756y | J. Am. Chem. Soc. 2012, 134, 8535–8542

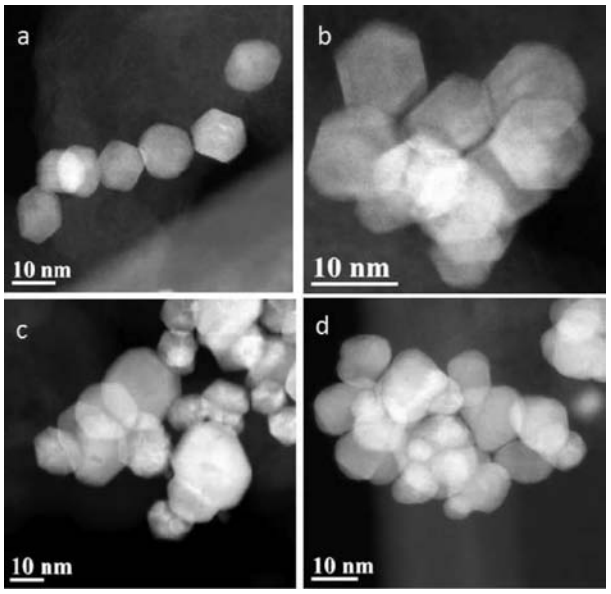

Figure 3. HAADF-STEM images of nanoparticles obtained from solvothermal syntheses with Pt/M = 3, where M is (a) Co from $Co(acac)_2$, (b) Co from $Co(acac)_3$, (c) Cu, and (d) Fe.

indicating a somewhat more complete reduction of the platinum precursor than of the nickel precursor. Surprisingly, a comparison of the XRD spectra of the products shows that while the NPs produced from a Pt/Ni reactant ratio of 3 comprised a single phase, nominally Pt_3Ni, syntheses with Pt/Ni reactant ratios of 2 or less gave products comprising two Pt–Ni phases. Figure 4 shows a representative spectrum of

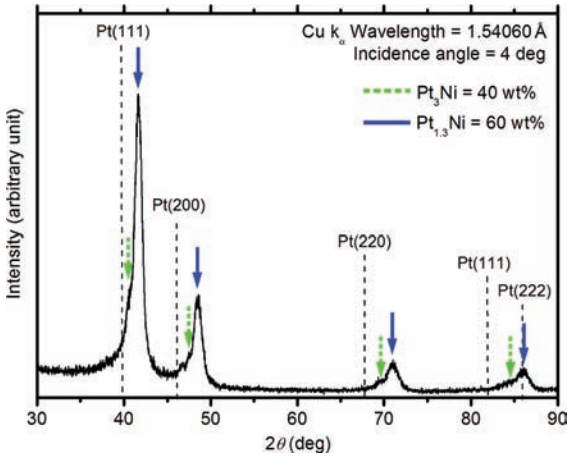

Figure 4. XRD spectra of nanoparticles from a DMF solvothermal reaction with a Pt/Ni molar ratio of 1.

such a dual-phase product obtained from a Pt/Ni reactant ratio of one. Rietveld refinement analysis indicates that this product was nominally composed of $Pt_{76}Ni_{24}$ and $Pt_{57}Ni_{43}$, with the latter phase accounting for about 60 wt % of the crystalline material. Rietveld refinement results for the products obtained from the various Pt/Ni ratios are given in Table 3.

In addition to the formation of two phases, the morphologies of the NPs were also affected as the reactant ratio decreased. From a mixture of cubic and cuboctahedral particles for a Pt/Ni ratio of 3, the predominant particle shapes shifted toward largely octahedral and truncated octahedral particles for lower Pt/Ni ratios. This trend is exemplified by the STEM images in Figure 5, which shows NPs produced from reaction mixtures having Pt/Ni ratios of 3 and 1.

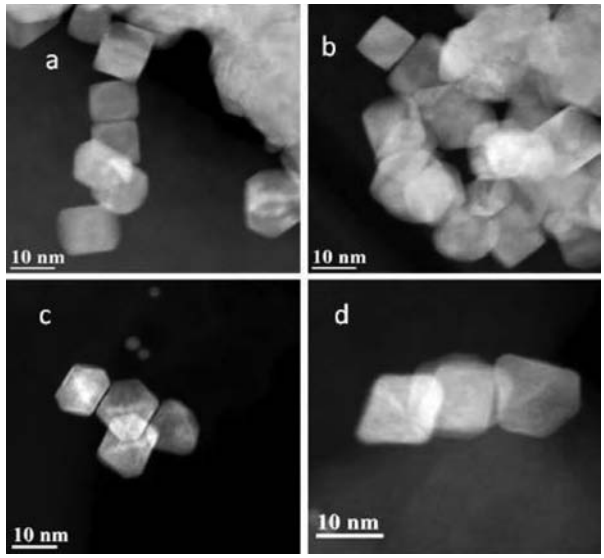

Figure 5. Comparison of HAADF-STEM of nanoparticles from DMF solvothermal reactions with a Pt/Ni molar ratio of 3 (a and b) and 1 (c and d).

Composition, Structure, and ORR Activity of Pt Alloy Nanoparticles. The ORR activities of the various catalysts were measured using a thin film RDE (TF-RDE) method similar to that reported by Schmidt and co-workers,[16] and electrochemical surface areas (ECSAs) were determined by integration of the current due to reversible hydrogen adsorption in a 0.1 M $HClO_4$ solution. The ECSAs for the Pt_3M alloys were typically near 20 m^2/g_{Pt}, while the ECSAs increased somewhat for the Pt–Ni alloys as their Pt/Ni ratio decreased. Thus, a maximum ECSA of 34 m^2/g_{Pt} was found for the product with a Pt/Ni ratio of 0.5. (Specific values can be found in the Supporting Information.)

The ORR specific activities of the carbon-supported Pt_3M alloy catalysts were between 600 and 800 $\mu A/cm^2_{Pt}$, well above the 200 $\mu A/cm^2_{Pt}$ seen for a Pt-on-carbon (Pt/C) standard. The Pt_3Ni catalyst performed somewhat better, with a specific activity of 1040 $\mu A/cm^2_{Pt}$. However, due to the generally larger particle sizes and resulting lower ECSAs versus the Pt/C standard, the mass activities of the Pt alloy catalysts were only somewhat greater than those of the standard. Nanoparticle agglomeration of the Pt alloys, seen by TEM, also contributed to a lower active surface area.

Figure 6 shows the ORR activities for the Pt–Ni alloy catalysts obtained from the various Pt/Ni reactant ratios. (The analyzed ratios are reported in the Supporting Information.) It can be seen that the specific activity increased nearly 3-fold as the Pt/Ni reactant ratio was reduced from 3 to 1. For this latter material, the specific activity was nearly 3000 $\mu A/cm^2_{Pt}$, or about 15 times that of the Pt/C standard, which is exceptional for a nanoparticle catalyst. The corresponding mass activity of this catalyst was 0.68 A/mg_{Pt}, greater than 5 times that of the Pt/C standard.

From the results of Rietveld analysis given in Table 3, it is clear that this surprising catalyst, with a nominal composition of PtNi, is actually a mixture of two alloy phases. Of particular

dx.doi.org/10.1021/ja300756y | J. Am. Chem. Soc. 2012, 134, 8535–8542

Table 3. Metal Content and Rietveld Analysis of C-Supported Pt_xNi_{1-x} Products

	analyzed metal content			XRD-derived values				
reactant Pt/Ni molar ratio	wt % Pt	wt % Ni	Pt/Ni molar ratio	lattice parameter (Å)	Ni mole fraction	Pt mole fraction	phase wt %	average crystallite size (nm)
0.5	23	11.8	0.6	3.7939	0.33	0.77	37	3.8
				3.7368	0.47	0.53	63	6.1
1	25	8.5	0.9	3.8292	0.24	0.76	40	6.7
				3.7529	0.43	0.57	60	6.7
1.5	27	4.8	1.7	3.8556	0.17	0.83	32	4.0
				3.7840	0.35	0.65	68	7.4
2	27	3.8	2.1	3.8636	0.15	0.85	61	3.1
				3.7976	0.32	0.68	39	5.9
3	29	2.7	3.2	3.8427	0.20	0.80	100	5.5

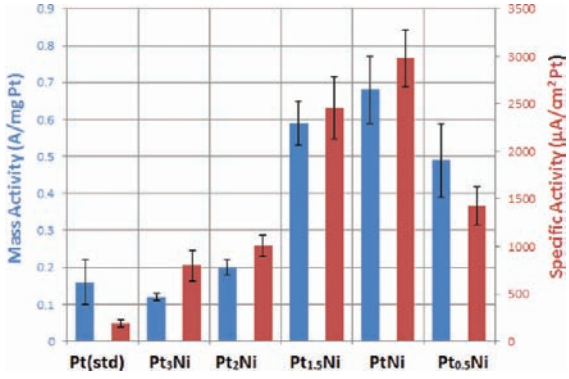

Figure 6. ORR activities of DMF-synthesized Pt–Ni nanoparticle catalysts. Bar colors correlate with axis label colors. Bar pairs are labeled with corresponding metal precursor ratios. Error bars show 95% confidence level.

interest then are the relative contributions of each phase to the ORR activity. Are both phases comparable in activity, or is one much more active than the other?

To better describe the individual particle types, HAADF imaging coupled with EDS analysis/mapping was used to examine the overall composition of and metal distribution within a number of PtNi nanoparticles. A typical example of such analysis is shown in Figure 7. This and similar figures strongly suggest the presence of Pt-rich surface layers on at least some of the particles. This is most evident in Figure 7 when comparing the regions of the Pt and Ni maps where two particles are in contact with each other. There the Ni intensity falls to essentially zero, while the Pt signal is quite robust. Looking at overall particle compositions, it was found that each NP actually falls into one of two composition ranges rather than adhering strictly to one of the two specific Pt–Ni compositions given by XRD–Rietveld analysis. Specifically, the nickel contents of PtNi NPs were found to be in one of two ranges: either 40–47 atomic % or 30–36 atomic %.

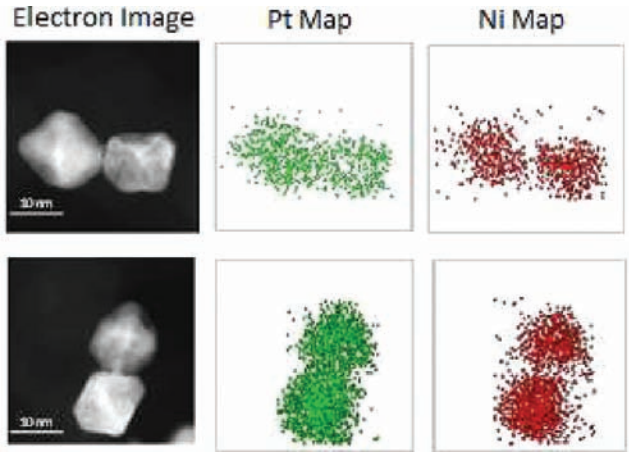

Figure 7. HAADF images and Pt and Ni EDS maps of fresh Pt–Ni nanoparticles. Colored pixels indicate where the element was detected above background.

Recent work by Wang et al.[22] has shown that Pt–Ni NPs can undergo significant Ni dissolution during the ORR activity testing procedure, which typically includes some initial electrochemical voltage cycling. Therefore, TEM images and EDS maps of our PtNi alloy NPs were obtained after ORR testing. From Figure 8, which shows TEM images of both fresh and ORR-tested PtNi catalysts, it is obvious that a number of NPs were significantly changed during the ORR testing protocol, developing significant voids or hollows. Presumably these voids were the result of nickel dissolution, although it is unclear whether or not exposure to the oxidizing potentials of ORR testing was required for significant dissolution. While a number of NPs from the ORR-tested catalyst are seen to have acquired voids, many other particles appear to be untouched.

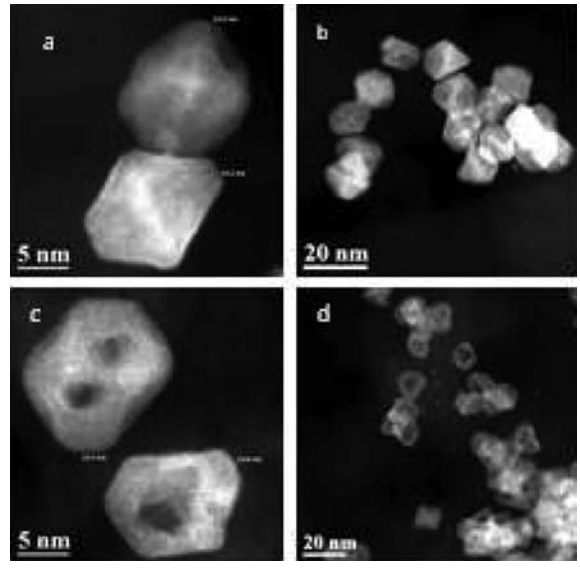

Figure 8. HAADF-STEM images of PtNi catalyst before (a and b) and after (c and d) TF-RDE measurements of ORR activity.

dx.doi.org/10.1021/ja300756y | J. Am. Chem. Soc. 2012, 134, 8535–8542

Interestingly, many of the particles with voids retained a high degree of faceting; that is, the hollowing process appeared to occur largely on (and into) the crystal faces, rather than disturbing the crystal edges.

Given that the fresh NPs have a nickel content in one of two ranges, it seems reasonable that one compositional range might be more susceptible to Ni dissolution than the other. EDS analysis of hollowed PtNi particles indicates that these NPs have nickel contents ranging from 14% to 25%. This is well below the nickel contents found in any of the fresh particles and confirms that void formation is due to the loss of Ni. EDS analysis of particles that were apparently unaffected by Ni dissolution, as seen by a lack of void formation, has shown them to have Ni contents in the Ni-rich range (40−47% Ni) found for fresh particles. Thus, it is tempting to speculate that the more Ni-rich NPs are actually more resistant to Ni dissolution than NPs in the region of lesser Ni content. We are pursuing further experiments to determine the validity of this hypothesis.

Because the PtNi catalyst sample used for ORR measurements was removed from the electrolyte immediately after ORR testing, it is clear that both types of particles, hollowed and solid, contributed to the measured activity. What is not clear, however, is which type of particle, hollowed or solid, contributes most to the high activity. Several recent papers on Pt−Ni catalyst materials, both experimental and theoretical, have dealt with the dependence of ORR activity on Pt−Ni composition and have concluded that maximum ORR activities occur in the range of 40−50 atomic % of nickel.[22−25] Such findings tend to support the position that the intact NPs of the catalyst, which retain a high nickel content, are most responsible for the overall high activity. Alternatively, many dealloyed catalysts have been shown to have exceptional activity by Strasser and co-workers.[26−29] Thus, the dealloyed, hollowed particles might instead be the source of the high activity. Potentially important to the activity of both particle types may be the well-faceted octahedral-based structures, particularly for the solid particles, which present a number of (111) surfaces that may be especially active. Also, the relatively large particle sizes of the catalyst NPs as compared to more conventional catalysts are expected to give higher specific activities.[1,30] Clearly, further work is needed to discriminate which particle types and specific attributes are responsible for the impressive activities of the PtNi catalyst.

Durability of the PtNi Catalyst. To determine the relative durability of the PtNi catalyst, the ORR activity of a catalyst thin film was measured before and after being subjected to 20,000 voltage cycles. Figure 9 shows the anodic scans used to determine the ORR activities of the fresh and cycled PtNi catalyst. While the specific activity of the PtNi catalyst film decreased by one-half after voltage cycling, from 2800 to 1400 $\mu A/cm^2_{Pt}$, the mass activity decreased by only 40% due to an increase in the ECSA from 26 to 31 m^2/g_{Pt}. This increase in surface area is the result of continued void formation in the catalyst NPs with cycling. This can be seen in Figure 10, which shows a typical micrograph of the cycled material. Examination of similar micrographs shows little change in average particle size and reveals that about 80% of the particles had significant hollows. EDS analysis confirms a significant loss of nickel from the cycled particles. Specifically, analysis of a number of particles indicates an average Ni content of about 20 atomic %. EDS mapping of the metals, as shown in Figure 10, indicates that the Ni remaining in each particle is fairly uniformly

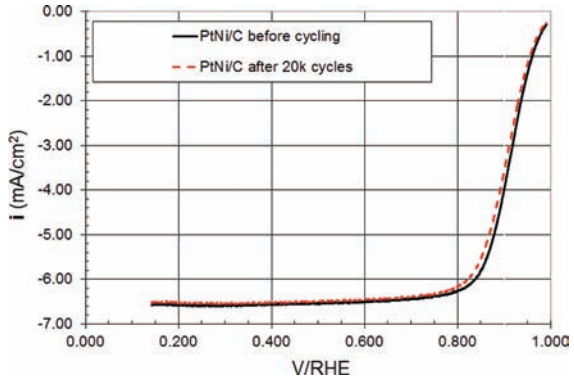

Figure 9. Polarization curves for ORR at 1600 rpm before and after 20 000 voltage cycles (between 0.6 and 1.0 V at 50 mV/s). Initial Pt loading of 19 $\mu g_{Pt}/cm^2$.

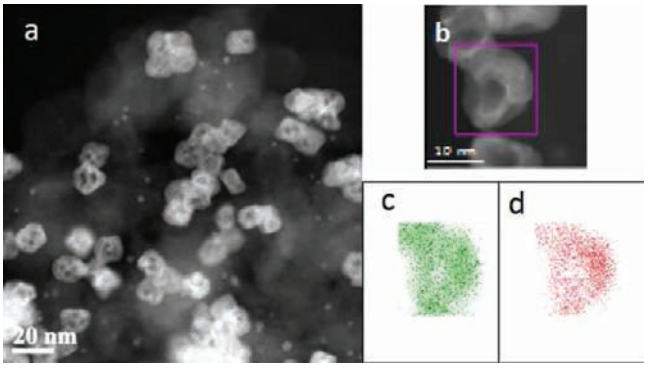

Figure 10. HAADF image of (a) 20k-cycled PtNi catalyst and (b) nanoparticle used for EDS mapping of (c) Pt and (d) Ni distribution within the nanoparticle. Colored pixels indicate where the element was detected above background.

distributed throughout the particle. It is also interesting to note that despite the intensive cycling, all of the hollowed particles retained a significant Ni content of at least 12%. This may indicate that there is a residual level of nickel content that will not be removed by further cycling. EDS analysis of several particles without voids gave an average nickel content of about 31% Ni.

One change that often occurs in nanoparticle catalysts with voltage cycling is a growth in particle size. For the PtNi catalyst cycled here, we find from TEM measurements that the average particle size is virtually unchanged with cycling, with an average of 14.5 nm seen for the fresh particles and 14.7 nm seen for the cycled NPs. Thus, neither particle fragmentation nor particle growth occurs significantly as the result of voltage cycling. Instead, the major structural effect of extended voltage cycling is the continued hollowing out of the faceted NPs due to Ni dissolution. The concomitant decrease in ORR specific activity with cycling suggests that these two effects may be linked, supporting the notion that the ORR activity of the hollowed particles is inferior to that of the solid, faceted particles.

■ SUMMARY

The solvothermal synthesis of Pt alloy nanoparticles using *N*,*N*-dimethylformamide as both solvent and reductant provides a useful platform for catalyst development. Well-faceted NPs of Pt_3Ni and Pt_3Co were successfully synthesized without capping agents and were found to have ORR specific activities 3−5 times greater than that of a Pt standard catalyst. Pt−Ni

dx.doi.org/10.1021/ja300756y | J. Am. Chem. Soc. 2012, 134, 8535−8542

nanoparticle morphology was strongly affected by the Pt/Ni reactant ratio, changing from predominantly well-faceted cubes and cuboctahedra to predominantly octahedra and truncated octahedra as the Pt/Ni ratio was changed from 3 to 1. NPs from reactions with Pt/Ni ratios of 2 or less were found to contain two Pt−Ni alloy compositions, in contrast to the single composition of NPs from a Pt/Ni ratio of 3. Also, the activities of the Pt−Ni NPs were found to increase as the Pt/Ni reactant ratio was decreased from 3 to 1, with the Pt/Ni = 1 product showing exceptional ORR activity. HAADF-STEM of this catalyst after ORR testing showed the formation of voids in many of the particles. Further voltage cycling generated voids in about 80% of the particles and decreased the mass activity by nearly 40%. Despite this decrease, the activity of this catalyst still nearly meets the DOE 2015 target for fresh catalyst activity. Further work is underway to determine which aspects of these catalysts are responsible for their high activity and to determine their long-term stability under fuel cell operating conditions.

■ ASSOCIATED CONTENT

Supporting Information

Additional reactions, ECSA and ORR measurements, and supplementary particle imaging. This material is available free of charge via the Internet at http://pubs.acs.org.

■ AUTHOR INFORMATION

Corresponding Author

michael.k.carpenter@gm.com

Notes

The authors declare no competing financial interest.

■ ACKNOWLEDGMENTS

We would like to acknowledge Nicholas Irish for ICP analysis, Michael Balogh and Vic Liu for helpful discussions, and Indrajit Dutta for initial imaging results.

■ REFERENCES

(1) Gasteiger, H. A.; Kocha, S. S.; Sompalli, B.; Wagner, F. T. *Appl. Catal., B: Environ,* **2005**, *56*, 9.
(2) Mukerjee, S.; Srinivasan, S. *J. Electroanal. Chem.* **1993**, *357*, 201.
(3) Soderberg, J. N.; Sirk, A. H. C.; Campbell, S. A.; Birss, V. I. *J. Electrochem. Soc.* **2005**, *152*, A2017.
(4) Toda, T.; Igarashi, H.; Watanabe, M. *J. Electroanal. Chem.* **1999**, *460*, 258.
(5) Zhang, J.; Mo, Y.; Vukmirovic, M. B.; Klie, R.; Sasaki, K.; Adzic, R. R. *J. Phys. Chem. B* **2004**, *108*, 10955.
(6) Adzic, R. R.; Zhang, J.; Sasaki, K.; Vukmirovic, M. B.; Shao, M.; Wang, J. X.; Nilekar, A. U.; Mavrikakis, M.; Valerio, J. A.; Uribe, F. *Top. Catal.* **2007**, *46*, 249.
(7) Wang, C.; van der Vliet, D.; More, K. L.; Zaluzec, N. J.; Peng, S.; Sun, S.; Daimon, H.; Wang, G.; Greeley, J.; Pearson, J.; Paulikas, A. P.; Karapetrov, G.; Strmcnik, D.; Markovic, N. M.; Stamenkovic, V. R. *Nano Lett.* **2011**, *11*, 919.
(8) Bonakdarpour, A.; Wenzel, J.; Stevens, D. A.; Sheng, S.; Monchesky, T. L.; Lobel, R.; Atanasoski, R. T.; Schmoeckel, A. K.; Vernstrom, G. D.; Debe, M. K.; Dahn, J. R. *J. Electrochem. Soc.* **2005**, *152*, A61.
(9) Liu, G. C.-K.; Burns, C.; Sanderson, R.; Stevens, D. A.; Vernstrom, G.; Atanasoski, R. T.; Debe, M. K.; Dahn, J. R. *ECS Trans.* **2010**, *33*, 153.
(10) Stamenkovic, V. R.; Fowler, B.; Mun, B. S.; Wang, G.; Ross, P. N.; Lucas, C. A.; Markovic, N. M. *Science* **2007**, *315*, 493.
(11) Wu, J.; Peng, Z.; Yang, S.; Yang, H.; Zhang, J.; Wagner, F. T. *J. Am. Chem. Soc.* **2010**, *132*, 4984.
(12) Zhang, J.; Yang, H.; Fang, J.; Zou, S. *Nano Lett.* **2010**, *10*, 638.
(13) Pastoriza-Santos, I.; Liz-Marzán, L. M. *Langmuir* **1999**, *15*, 948.
(14) Jeong, G. H.; Kim, M.; Lee, Y. W.; Choi, W.; Oh, W. T.; Park, Q.-H.; Han, S. W. *J. Am. Chem. Soc.* **2009**, *131*, 1672.
(15) Cullity, B. D. *Elements of X-Ray Diffraction*; Addison-Wesley Publishing Co.: Reading, MA, 1978.
(16) Schmidt, T. J.; Gasteiger, H. A.; Stab, G. D.; Urban, P. M.; Kolb, D. M.; Behm, R. J. *J. Electrochem. Soc.* **1998**, *145*, 2354.
(17) Pastoriza-Santos, I.; Liz-Marzán, L. M. *Langmuir* **2002**, *18*, 2888.
(18) Pastoriza-Santos, I.; Liz-Marzán, L. M. *Nano Lett.* **2002**, *8*, 903.
(19) Deivaraj, T. C.; Chen, W.; Lee, J. Y. *J. Mater. Chem.* **2003**, *13*, 2555.
(20) Moffat, T. P.; Mallett, J. J.; Hwang, S.-M. *J. Electrochem. Soc.* **2009**, *156*, B238.
(21) Narayanan, R.; El-Sayed, M. A. *J. Phys. Chem. B* **2004**, *108*, 5726.
(22) Wang, C.; Chi, M.; Wang, G.; van der Vliet, D.; Li, D.; More, K.; Wang, H.-H.; Schlueter, J. A.; Markovic, N. M.; Stamenkovic, V. R. *Adv. Funct. Mater.* **2011**, *21*, 147.
(23) Yang, H.; Vogel, W.; Lamy, C.; Alonso-Vante, N. *J. Phys. Chem. B* **2004**, *108*, 11024.
(24) He, T.; Kreidler, E.; Xiong, L.; Ding, E. *J. Power Sources* **2007**, *165*, 87.
(25) Matanović, I.; Garzon, F. H.; Henson, N. J. *J. Phys. Chem. C* **2011**, *115*, 10640.
(26) Koh, S.; Leisch, J.; Toney, M. F.; Strasser, P. *J. Phys. Chem. C* **2007**, *111*, 3744.
(27) Koh, S.; Hahn, N.; Yu, C.; Strasser, P. *J. Electrochem. Soc.* **2008**, *155*, B1281.
(28) Mani, P.; Srivastava, R.; Strasser, P. *J. Phys. Chem. C* **2008**, *112*, 2770.
(29) Strasser, P.; Koh, S.; Greeley, J. *Phys. Chem. Chem. Phys.* **2008**, *10*, 3670.
(30) Wang, C.; Wang, G.; van der Vliet, D.; Chang, K.-C.; Markovic, N. M.; Stamenkovic, V. R. *Phys. Chem. Chem. Phys.* **2010**, *12*, 6933.